

Probing the Solar Corona at High Temporal and Spatial Resolution with the LOw Frequency ARray (LOFAR)

A dissertation submitted to the University of Dublin
for the degree of Doctor of Philosophy

Pearse Murphy, B.A. (Mod.)
School of Physics, Trinity College Dublin

Supervisor:
Prof. Peter T. Gallagher
Co-Supervisor:
Dr. Eoin P. Carley

December 2021



Trinity College Dublin
Coláiste na Tríonóide, Baile Átha Cliath
The University of Dublin

Summary

The solar corona is the outermost layer of the Sun's atmosphere. Advancements in radio astronomy over the last 50 years have revealed a number of radio phenomena which occur in the corona each with different temporal and spectral characteristics. Current generation interferometers such as the Low Frequency ARray (LOFAR) give an unprecedented insight into the fine structure of these radio bursts. Of particular interest are what are known as Type III radio bursts. These are indicative of electrons being accelerated along open magnetic field lines in the solar corona. Particularly bright radio bursts can have devastating effects on terrestrial communication including GPS positioning and satellite communication. Given that much of modern society relies on satellite communication, being better able to understand and perhaps predict radio bursts is essential. High temporal resolution data allow the study of rapid temporal variability in radio spectra which are indicative of small-scale turbulence in the solar corona. It is thought that the density inhomogeneities produced by this small-scale turbulence causes scattering of radio waves as they propagate out from the corona and thus pose a fundamental limit on the source size of observed radio bursts. Analysis of a radio burst at the plasma frequency, such as a Type III burst, with highly spatially resolved interferometric data is the most direct way of testing this hypothesis.

The nature of this PhD is twofold, firstly to observe low frequency radio emission from the Sun at spatial resolution of the order of 15 arcseconds. This will determine whether or not scattering of radio waves in the corona imposes a fundamental limit on spatial resolution and give insight into the processes that might cause this limit. The second aspect of this PhD is to observe the Sun at radio wavelengths at the highest temporal resolution ever. In order to do this, the TBB Acquisition Cluster (TACl) located in the I-LOFAR control room must be further developed to record and store TBB data without corruption. Observing the Sun at nanosecond temporal resolution has yet to be attempted and as such the potential to discover new radio phenomena and temporal variability in existing phenomena is great. It is, of course, possible that such events do not occur or are difficult to detect and as such the focus for this PhD will lie mainly on interferometric observations of the Sun.

This report is an overview of my PhD thus far and is as follows. Chapter 1 describes the Sun and the corona. It introduces the role radio bursts have to play in determining source sizes in the corona and outlines the theory behind plasma emission, radio interferometry and beam-forming. Chapter ?? gives a technical description of LOFAR, its hardware and the digital signal processing pipeline of an international LOFAR station. Observations using high temporal resolution data from I-LOFAR are explained in chapter ?? along with interferometric images from the core and remote LOFAR stations. The results of analysis of this data is also given in chapter ?? before the report is concluded in ??. Future work for this PhD is outlined in chapter ??.

Declaration

I have read and I understand the plagiarism provisions in the General Regulations of the University Calendar for the current year, found at: <https://www.tcd.ie/calendar>

I have also completed the Online Tutorial on avoiding plagiarism 'Ready, Steady, Write', located at <http://tcd-ie.libguides.com/plagiarism/ready-steady-write>

I declare that this report is my own work, is not copied from any other person's work (published or unpublished), and has not previously submitted for assessment either at Trinity College Dublin or elsewhere.

Name: Pearse Murphy

Signature: **Date:**

List of Publications

Oral Presentations

1. *Finding Fast Solar Radio Transients in I-LOFAR Transient Buffer Board Data*, Irish National Astronomy Meeting (INAM), 2018
2. *Finding Fast Solar Radio Transients in I-LOFAR Transient Buffer Board Data*, Community of European Solar Radio Astronomers (CESRA) Summer School, 2018

Poster Presentations

1. *The Irish LOw Frequency ARray (I-LOFAR)*, International Workshop on Solar, Heliospheric and Magnetospheric Radioastronomy, 2017
DOI: <https://doi.org/10.6084/m9.figshare.5572660.v1>
2. *Nanosecond Sampling of the Radio Sky with I-LOFAR's Transient Buffer Boards (TBB)*, 17th RHESSI (Reuven Ramaty High Energy Solar Spectroscopic Imager) Workshop, 2018
DOI: <https://doi.org/10.6084/m9.figshare.6669173.v1>

Workshops & Conferences Attended

1. INAM, Maynooth University, 2017
2. International Workshop on Solar, Heliospheric and Magnetospheric Radioastronomy, Observatoire de Paris, 2017
3. I-LOFAR User's Data Workshop, University College Dublin, 2018
4. 17th RHESSI Workshop, Trinity College Dublin, 2018
5. Astro Hack Week, Lorentz Cetrre, Leiden University, 2018
6. INAM, Birr Theatre, Birr, Co. Offaly, 2018
7. CESRA Summer School, Observatoire Royal de Belgique, 2018
8. LOFAR Data Processing School, Netherlands Institute for Radio Astronomy (ASTRON), 2018

Publications

1. David M. Long, **Pearse C. Murphy**, Georgina Graham, Eoin P. Carley, David Pérez-Suárez.
“A Statistical Analysis of the Solar Phenomena Associated with Global EUV Waves”,
Solar Physics, Volume 292 , Issue 185, (2017).

Contents

List of Publications	iii
List of Figures	vi
1 Introduction	1
1.1 The Sun	1
1.1.1 The Corona	1
1.1.2 Solar Flares	2
1.1.3 Coronal Mass Ejections (CMEs)	4
1.1.4 Radio Phenomena in the Solar Corona	4
1.1.5 Type III Bursts	7
1.1.6 Source Sizes in the Corona	9
1.2 Plasma Emission	9
1.2.1 Generation of Langmuir Waves	10
1.2.2 Wave-Wave Interaction	11
1.3 Radio Interferometry	14
1.3.1 Beam-forming	16
References	17

List of Figures

1.1	Diagram of Sun's interior and atmospheric layers.	2
1.2	Model of electron density and temperature with height in the solar atmosphere.	3
1.3	GOES lightcurve for X9 class flare on 2017-09-10	3
1.4	CME observed with the LASCO C2 instrument on 2000-02-27. The blank area shows the extent of the coronagraph and the white circle represents the solar disk.	4
1.5	Cartoon of Type I-V radio bursts	5
1.6	A number of Type III bursts observed by Zucca et al. (2012) on 21 October 2011.	8
1.7	Langmuir wave distribution function and spectral energy density.	11
1.8	A three wave process of fundamental plasma emission $L \rightarrow T + S$	13
1.9	Three wave process of second harmonic plasma emission $L + L' \rightarrow T$	13
1.10	A two element interferometer	14

Introduction

1.1 The Sun

The Sun is our nearest star and the centre of our solar system. It is a G2 type star located on the main sequence of the Hertzsprung Russell diagram. It has a luminosity of $(3.84 \pm 0.04) \times 10^{26}$ W and a radius $R_{\odot} = (6.959 \pm 0.007) \times 10^8$ m. With a mass of $(1.9889 \pm 0.0003) \times 10^{30}$ kg, the Sun comprises $> 99\%$ of the solar system's total mass (Foukal, 2004). Formed from a cooling cloud of gas and dust 4.6 billion years ago, the Sun now has a core with a temperature of 15 MK, which enables nuclear fusion to occur.

The layer of the Sun at $1 R_{\odot}$ is known as the photosphere and is what would be called the surface of the Sun. Above the photosphere is the Sun's atmosphere consisting of the chromosphere, transition region and the corona. Figure 1.1 shows the interior layers of the Sun and its atmosphere.

1.1.1 The Corona

The outermost layer of the solar atmosphere is called the corona. It is a hot, tenuous plasma which displays a number of interesting phenomena thought to be governed by its complex magnetic field. The corona begins ~ 2500 km above the photosphere after a layer in the Sun's atmosphere known as the transition region, where electron density decreases and temperature increases dramatically (Figure 1.2). The electron density in the corona ranges from 10^9 cm^{-3} at the base to 10^6 cm^{-3} at distances of $1 R_{\odot}$ from the solar surface. Densities vary throughout the corona. Sparse, underdense regions at the base of the corona known as coronal holes exhibit densities of $\sim (0.5 - 1.0) \times 10^8 \text{ cm}^{-3}$ whereas areas of high magnetic activity known as active regions have electron densities of $\sim 2 \times 10^9 \text{ cm}^{-3}$.

Observing the white light corona is done with a number of ground-based and space-based instruments called coronagraphs, that emulate the effect of a total eclipse. The Large Angle and Spectrometric Coronagraph (LASCO) on board the Solar and Heliospheric Observatory (SOHO) is one such instrument and allows the corona to be observed from distances of $2\text{-}32 R_{\odot}$.

Energetic events in the corona such as solar flares and coronal mass ejections (CMEs), described in 1.1.2 and 1.1.3, are studied across the electromagnetic spectrum. They are studied in order to understand how particles are accelerated, how energy is released and ultimately, why the corona has such an unaccountably high temperature. Most particle acceleration events in the solar corona have a diagnostic in radio spectra. This PhD focuses on studying these radio diagnostics at their highest temporal and spatial resolutions to date.

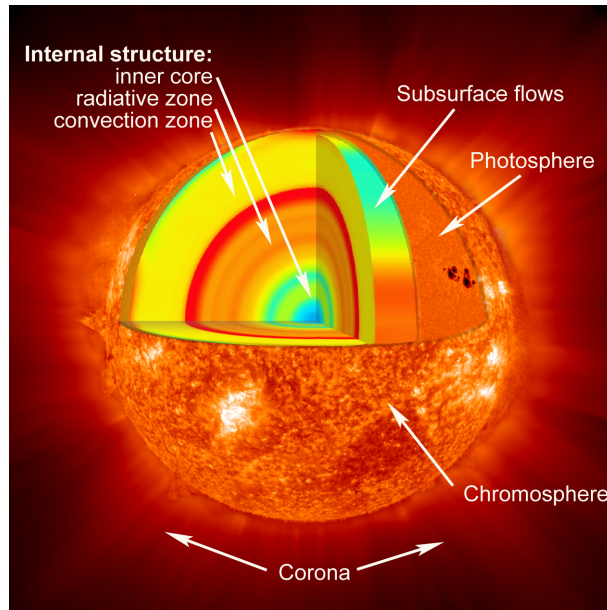


Figure 1.1: Diagram of Sun's interior and atmospheric layers. Photons produced by nuclear fusion in the core transfer energy outwards through the radiative zone to $0.7 R_{\odot}$. At this point, convection becomes the main form of energy transport. The visible surface of the Sun is known as the photosphere and marks the boundary between the interior and the atmosphere. The solar atmosphere consists of three layers, the chromosphere, the transition region (not shown) and the corona.

1.1.2 Solar Flares

Solar flares are massive releases of magnetic energy commonly believed to be due to a reconfiguration in the complicated magnetic field structure in an active region. They are some of the most energetic events in the solar system, releasing $\sim 10^{25}$ J of energy over a matter of minutes. Flares are observed across the electromagnetic spectrum from radio waves to γ rays with energies > 10 MeV. They are classified by the amount of X-ray flux (W m^{-2}) detected by the Geostationary Operational Environmental Satellite (GOES) 1-8 Å band on a logarithmic scale as being A, B, C, M or X class with A being the lowest flux (10^{-8} W m^{-2}) and X the highest (10^{-4} W m^{-2}). Each class is further subdivided into a linear scale. A timeseries of X-ray flux from a solar flare is often called a lightcurve and has three characteristic phases; a pre-flare phase which shows X-ray flux associated with the active region where the flare occurs, an impulsive phase showing a sharp rise in X-ray flux corresponding to accelerated particles colliding with the solar surface, and a gradual decay phase where plasma heated by the flare gradually cools back to its pre-flare state. Figure 1.3 shows a GOES light curve of the X9 class flare that occurred on 2017-09-10 and the three flare phases described above.

During solar flares, magnetic structures known as coronal loops fill with hot plasma and begin to emit in soft X-rays. At the same time, electrons are accelerated towards the solar surface where their energy is converted to hard X-rays in the collision via bremsstrahlung.

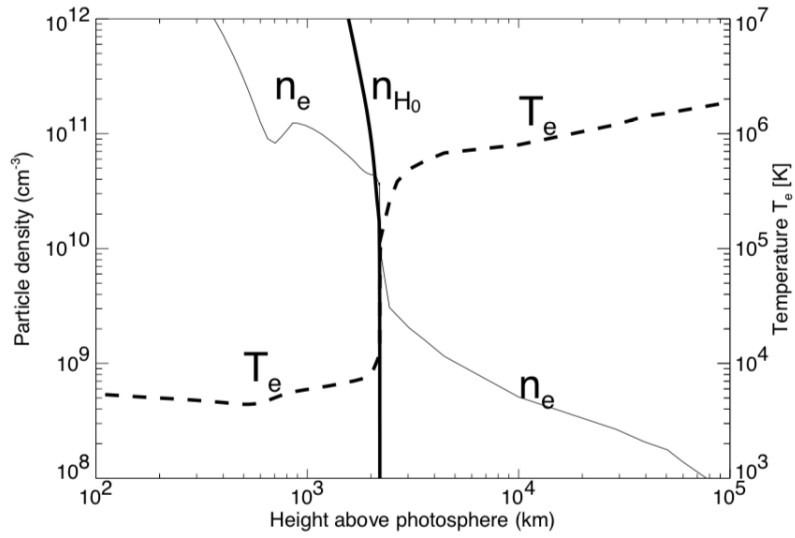


Figure 1.2: Model of electron density and temperature with height in the solar atmosphere. The region around 2000 km showing a sharp rise in temperature and sharp fall in electron density is known as the transition region, above this height plasma becomes fully ionised. Image taken from [Aschwanden \(2004\)](#)

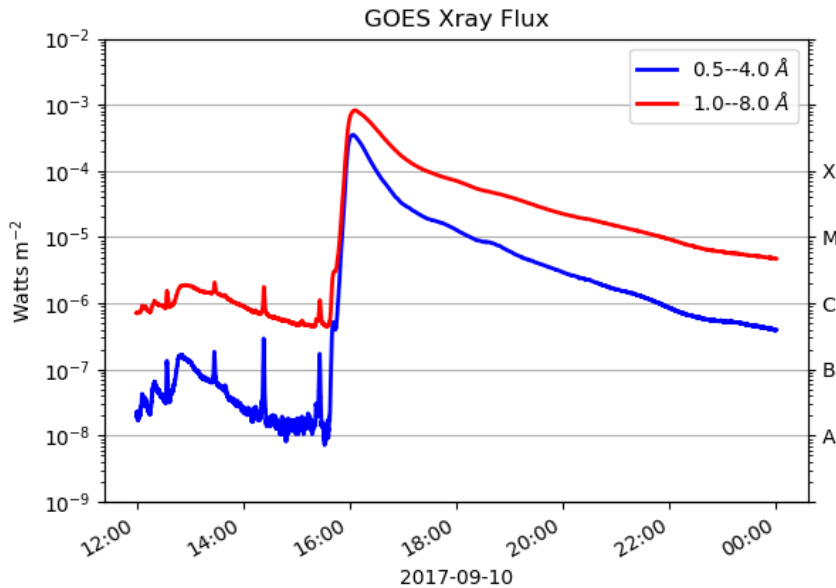


Figure 1.3: The GOES lightcurve of the X9 flare that occurred on 2017-09-10. The red curve shows the 1-8 Å channel by which the flare is classified while the blue curve shows the 0.5-4 Å band. The three characteristic phases of a solar flare are clearly displayed here. The pre-flare phase before ~ 16 : 00 UTC, the impulsive phase indicated by the sharp rise in flux and the gradual decay phase where X-ray flux gradually returns to the pre-flare level.

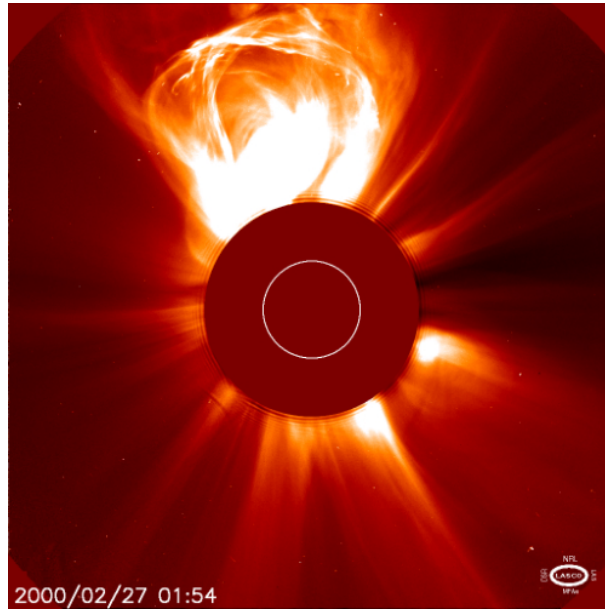


Figure 1.4: CME observed with the LASCO C2 instrument on 2000-02-27. The blank area shows the extent of the coronagraph and the white circle represents the solar disk.

1.1.3 Coronal Mass Ejections (CMEs)

In certain magnetic reconnection events, plasma suspended in a magnetic flux rope erupts from the corona into the heliosphere, the volume around the Sun where the interplanetary medium is dominated by particles flowing outward from the Sun. These eruption events are known as coronal mass ejections and accelerate 10^{15} g of charged particles at typical speeds of up to $\sim 2500 \text{ km s}^{-1}$ (Gopalswamy & Thompson, 2000). A “textbook” CME structure consists of a bright front that surrounds a dark cavity and a bright central core. CMEs are observed using coronagraphs as they are much fainter than the solar disk. An example of a CME observed using the LASCO C2 corona with a field of view from $1.5 R_{\odot}$ to $6 R_{\odot}$ can be seen in Figure 1.4. Ejected material from a CME can interact with the Earth’s magnetosphere and are known to have caused adverse effects including satellite communication disruption, radio blackouts, wide spread power outages and large inaccuracies in GPS positions. CMEs can travel faster than local Alfvén speed in the corona leading to a shock which can accelerate particles.

1.1.4 Radio Phenomena in the Solar Corona

Particles in the solar corona are accelerated by solar flares and CMEs, resulting in a range of radio bursts distinguish in spectra as the “classic” Type I-V radio bursts described by Wild (1950). A wealth of other fine structure radio bursts are also observed, predominantly found in radio storms such as S bursts, drift pairs and stria (McConnell, 1980; Melrose, 1982; Nelson & Melrose, 1985). The fine structure of these bursts can often reveal information about small-scale turbulence in the corona (Kontar et al., 2017) and

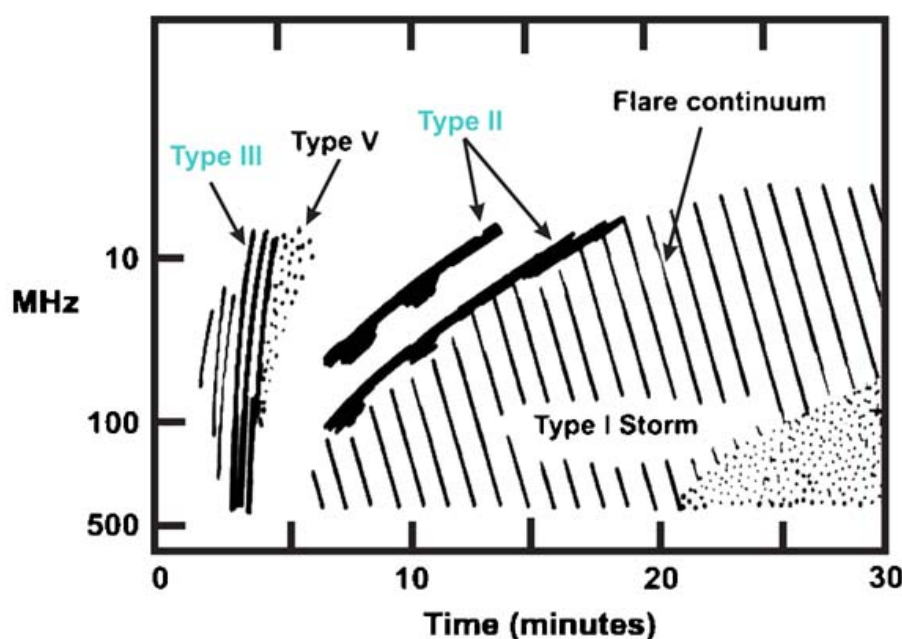


Figure 1.5: A cartoon of Type I-V radio bursts. Image taken from [Cliver & Ling \(2009\)](#)

offer the greatest chance of solving the coronal heating problem.

A brief description of some solar radio phenomena is given here while a more in depth review of the plasma emission process is given in appendix ??.

Type I bursts Type I emission can appear as bursts and/or a continuum originating from “storm centres” that are associated with active regions. Type I storms can last for many days. Emission from Type I bursts is highly circularly polarised in the o-mode (whereby light is circularly polarised in the same direction as electrons gyrating about a magnetic field line) and is also particularly directional with an increase in intensity as active regions rotate to the centre of the disk. Unlike Type II or III bursts, they do not exhibit a harmonic structure.

Type II bursts Type II radio bursts are a form of radio emission seen from the Sun and are identified by a slow ($\sim 0.1 \text{ MHz s}^{-1}$) drift to lower frequencies in dynamic spectra. The frequency drift can be used to find the velocity of the shock causing a burst if the electron number density as a function of height is known. The velocities of Type II bursts are often found to be $\sim 1000 \text{ km s}^{-1}$, much faster than the Alfvén velocity in the quiet corona, $\approx 270 \text{ km s}^{-1}$, meaning a shock must be present. Other basic properties of Type II bursts include:

1. Narrow bandwidths of up to $\sim 100 \text{ MHz}$ from initial to final frequencies.
2. A harmonic structure of two bands with a frequency ratio slightly less than 2:1 at a fundamental, f_p , and harmonic, $2f_p$, frequency can be seen for most Type II bursts.

This structure is consistent with the idea that Type II emission is due to plasma oscillations.

3. A large number of Type II bursts contain band splitting into an upper and lower band for each of the harmonics in their spectra. The cause for this splitting is not fully understood but it is commonly thought that the two bands are related to emission upstream and downstream of the MHD shock front which causes the Type II burst (Nelson & Melrose, 1985; Smerd et al., 1974; Vršnak et al., 2002).
4. Herringbone structure. Approximately 20% of Type II bursts show a herringbone structure of rapidly drifting emission spikes shooting out of the “backbone” of the main frequency drift to higher and lower frequencies. These herringbones are thought to be due to electron beams being accelerated at the associated shock for the Type II burst (Mann, 1995). While the backbone is poorly polarised, the herringbones have been found to be quite strongly, $\sim 70\%$, polarised. This is further evidence that herringbone structure is due to Type III-like emission from accelerated electron beams.
5. Starting emission frequencies of the order of a few 100 MHz ending at frequencies above 20 MHz. This being said, Type II burst with starting frequencies of ~ 100 kHz have also been observed. These lower frequency bursts are thought to be due to interplanetary shocks whereas higher frequency bursts are considered to be from shocks in the low corona.
6. Typical durations of 5-15 minutes. Type II bursts that occur after a flare do so with a delay ranging from 2-20 minutes. Bursts with shorter durations generally have higher starting frequencies.

Based on these and a number of other properties discussed in greater detail by Nelson & Melrose (1985), Type II radio bursts can be used as indicators for MHD shocks in the solar corona. Observational proof of frequency varying inversely with time in the solar wind, consistent with radiation being generated at f_p and $2f_p$ directly upstream from a CME-driven shock, was found by Reiner et al. (1997) and solidifies this argument.

Type IV burst Type IV bursts come in at least three sub-types with the general characteristic that they are of the form of broadband emission lasting for several hours. Early stationary Type IV bursts (also known as the flare continuum) associated with the decay phase of solar flares, late stationary bursts which appear similar to Type I emission, and moving Type IV bursts which exhibit a smooth, wide-band spectrum.

Type V burst The last of the broadband emission bursts, Type V radio bursts typically have a duration of 1-3 minutes and appear as an afterglow from Type III bursts. Type V emission is strictly less than 150 MHz and is accepted that it results from electrons that generate a Type III burst and become trapped in a closed magnetic loop in the corona.

Fine Structure: S bursts S bursts, initially called Fast Drift Storm (FDS) bursts, were first observed at the Culgoora Solar Observatory in 1967 (Ellis, 1969). They were later renamed by McConnell (1980) who likened them to Jovian S bursts. They have a narrow bandwidth of the order of 0.03 MHz and a drift rate of 1-2 MHz s⁻¹ and durations much less than 1s. McConnell (1980) also concluded that S bursts are radiated at either the plasma frequency or its harmonic in a manner similar to Type III bursts, see appendix ??, but that the implications of S burst fine structure and coronal scattering can only be defined once it is determined which harmonic of the plasma frequency they are radiated at. Melnik et al. (2010) propose a model of S bursts being generated by coalescence of fast magnetosonic waves with Langmuir waves which agrees well with the analysis of Clarke et al. (2019). Modern observations of S bursts, such as those conducted using LOFAR's tied-array imaging mode (Morosan et al., 2015), can give greater insight into the spectral and temporal variability of S bursts and what this might mean for the environment they are generated in.

1.1.5 Type III Bursts

Type III bursts are possibly the most useful radio burst for studying various aspects of the corona outlined later. Furthermore, section ?? describes a Type III burst that is being analysed as part of this PhD. Reid & Ratcliffe (2014) review a number of notable properties of Type III bursts. The defining characteristic of Type III bursts is a drift from high to low frequencies in a dynamic spectrum. The drift rates for Type III bursts are typically quite fast, of the order of ~ 10 MHz s⁻¹ depending on the frequency. The frequency drift rate, df/dt , has been found to have various relations with frequency (Reid & Ratcliffe, 2014) but most agree that $df/dt \propto f^\alpha$, where α varies depending on the study from ~ 1 to ~ 2.7 .

Ginzburg & Zhelezniakov (1958) proposed that Type III bursts are emitted at the plasma frequency,

$$\omega_p^2 = \frac{n_e e^2}{m_e \epsilon_0} \quad (1.1)$$

where n_e is the number density of electrons, m_e is the electron mass, e is the electron charge and ϵ_0 is the permittivity of free space. Although Eq. 1.1 is relatively simple, it contains an important principle of plasma physics. Namely, the plasma frequency is proportional to the square root of the electron density. This means that plasmas at higher

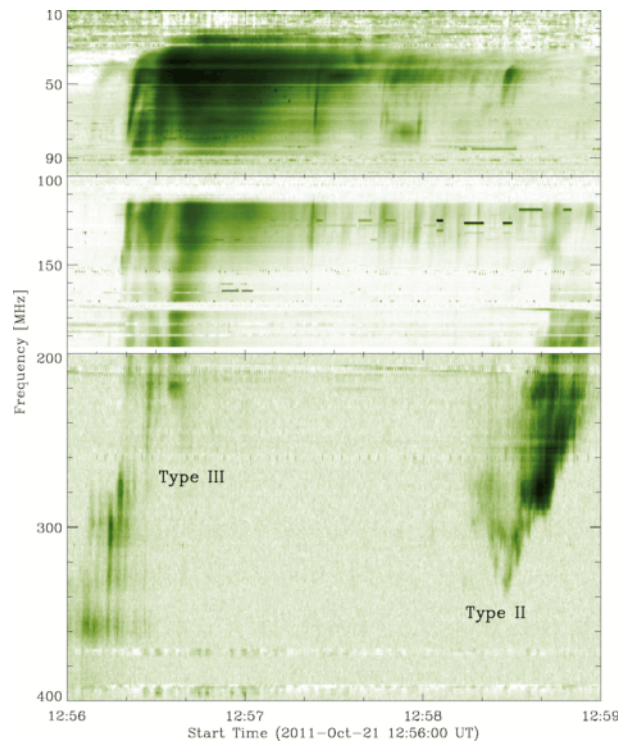


Figure 1.6: A number of Type III bursts observed by [Zucca et al. \(2012\)](#) on 21 October 2011. Note the Type III storm below 200 MHz and the Type II burst between 140 and 330 MHz.

electron densities will oscillate at higher frequencies than those of lower densities. The drift in Type III bursts, which are emitted at ω_p , is therefore an indication of the emission source moving from an area of high electron density, the photosphere, to low density, the upper corona.

Type III bursts are observed to be in two bands, a fundamental and harmonic band that are emitted at ω_p and $2\omega_p$ respectively. Both bands exhibit the same frequency drift although the flux of the harmonic band is usually less than that of the fundamental band. The process of plasma emitting radio frequencies at ω_p and $2\omega_p$ will be explained in more detail in section 1.2.2.

Figure 1.6 shows Type III radio bursts below 400 MHz observed by [Zucca et al. \(2012\)](#). A Type II burst was also observed between 140 and 330 MHz and exhibits a much slower frequency drift than the Type III bursts. A Type III storm can be seen below 200 MHz. This is when Type III emission is continuous over the span of large time scales and can last days. Type III bursts come in a number of subcategories described below.

Reverse and bi-directional bursts A typical Type III burst is produced when an electron beam travels along a magnetic field line away from the Sun to areas of lower density. During the magnetic reconnection process that accelerates these electrons, some electrons travel towards the Sun to areas of higher density and thus have a reversed frequency drift. Bursts where both the regular and reverse drifts can be seen simultaneously

are bi-directional bursts.

Type IIIb bursts While typical Type III bursts have smooth emission, Type IIIb bursts contain a fragmented substructure. This substructure is in the form of a chain of emission bands/striae that drift in frequency as a whole but individually show little frequency drift.

Type U and J bursts In the case where electrons are travelling along a closed magnetic field line, a turning point in the frequency drift of a Type III burst can be observed. For electrons that generate radio emission down to the footpoint of the magnetic field line, a U burst is observed. A U burst can be identified as an inverted U on a dynamic spectrum. More often, electrons stop generating radio emission as they travel back down the magnetic field line so only the turning point in frequency drift is visible in dynamic spectra. These are known as J type bursts. The reason for higher occurrence of J bursts compared to U bursts is described by [Reid & Kontar \(2017\)](#).

1.1.6 Source Sizes in the Corona

Analysis of short temporal bursts with small bandwidths suggest source sizes in the corona to be of the order ~ 6000 km ([McConnell, 1980](#)). Radio images of the Sun at metric and decametric wavelengths have yet to reveal this level of spatial structure. This is mostly due to the limit of resolution obtainable with modern interferometers however, the suggestion that there is a fundamental limit imposed upon the level of resolution obtainable by scattering in a turbulent corona ([Bastian, 1994](#)) has gathered a following in recent years ([Kontar et al., 2017](#)). [Riddle \(1974\)](#) described the effect of scattering in a spherically symmetric corona with random isotropic inhomogeneities with and without density enhancements due to streamers. Here they showed that the “directivity pattern”, the ratio of the power received from a source with and without scattering, was significantly broadened for radio bursts near the local plasma frequency, 80 MHz in their case. Sub-arcminute interferometric observations of Type III radio bursts could give a definitive answer to this question.

1.2 Plasma Emission

In 1942 while Britain was on the look out for radar signals of enemy aircraft, a strong, noise like and highly variable signal was noticed by radar operators. Initially it was thought that Germany had managed to learn the secret of radar and create some sort of jamming device. On further investigation it was found that this jamming was in fact radio emission from the Sun. The discovery of this radio emission being associated with

a major solar flare was kept secret until after the war and was published by [Appleton & Hey \(1946\)](#). Since then a number of major advancements in both instrumentation and theory have occurred. A culmination of the theory of solar radio emission is laid out in the book by [McLean & Labrum \(1985\)](#) while worldwide, a number of extraordinary radio telescopes and interferometers such as the LOw Frequency ARray (LOFAR, ? ?), the Nançay Radio Heliograph and the Murchison Widefield Array (MWA), to name but a few, have been built.

Solar radio emission often comes in the form of bursts of varying timescales. These were initially classified into three types by [Wild & McCready \(1950\)](#) with a fourth and fifth type being discovered by [Boischot & André \(1957\)](#) and [Wild et al. \(1959\)](#) respectively. Of these, the most frequently occurring are the so called Type III radio bursts. These are short bursts that can be observed over many frequencies and are found to be associated with solar flares ([Malville & M., 1962](#)). An initial study into how they are emitted was conducted by [Ginzburg & Zhelezniakov \(1958\)](#).

For a Type III radio burst to be emitted, an electron must generate Langmuir waves in the plasma. These Langmuir waves then go on to generate electromagnetic transverse waves by coalescing with other waves or by decaying. These electromagnetic waves are the radio bursts that are observed. In this section the generation of Langmuir waves and the process of plasma emission are discussed.

1.2.1 Generation of Langmuir Waves

During magnetic reconnection in a solar flare electrons are accelerated along magnetic field lines. As these beams of electrons propagate, faster electrons begin to outpace slower electrons and stationary ions in the background plasma. This leads to a second peak on the Maxwell Boltzmann distribution of velocities as seen in Figure 1.7. Energy is transferred from electrons travelling at the phase velocity, v_ϕ , to Langmuir waves creating a resonance. The positive velocity gradient of this resonance means that there are more electrons with velocity greater than v_ϕ than there are electrons with velocities less than v_ϕ (where energy is transferred from the wave to the particles), this causes Langmuir waves to become unstable and their magnitudes to grow exponentially. Particles with velocities near v_ϕ are in resonance with the Langmuir waves and drive this instability.

This instability is alleviated by what is known as quasi-linear relaxation ([Melrose, 1987](#)) whereby the resonant behaviour of the electrons and Langmuir waves results in a plateau in the Maxwell Boltzmann distribution rather than a second peak. It can be shown that ([Vedenov, 1963](#)) the electron distribution function, $f(v, t)$ where $\int f(v, t) dv = n_e$, and the spectral energy index of Langmuir waves, $W(v, t)$ such that $\int W(v, t) dv = E_L$

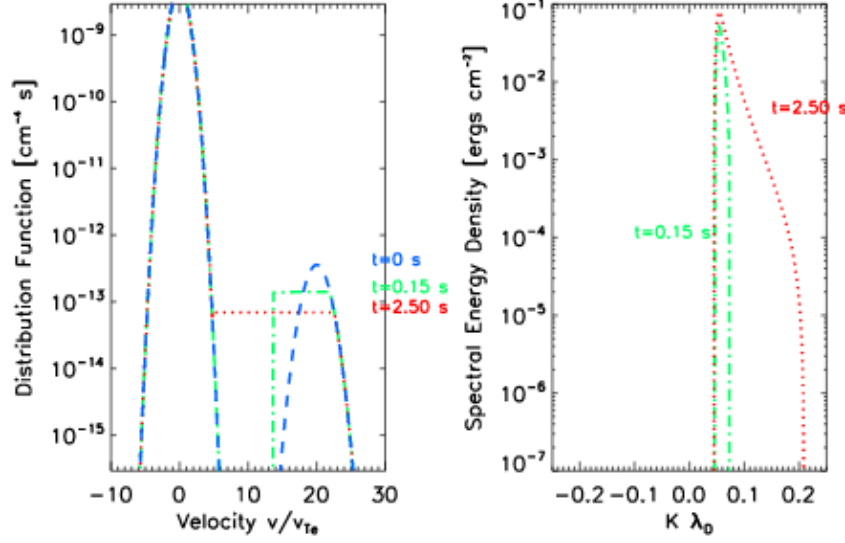


Figure 1.7: Left: Evolution of distribution function (normalised by the electron thermal velocity $v_{Te} = V_e$) in time. The diffusive term in 1.2 causes the bump-on-tail Gaussian to turn into a plateau, thereby eliminating the instability caused by the positive velocity gradient. Right: The spectral energy density of generated Langmuir waves, x-axis normalised to the Debye length $\lambda_D = \sqrt{\frac{\epsilon_0 k_B T_e}{e^2 n_e}}$. As time passes the spectral range of Langmuir waves increases. Each panel shows successive times of $t=0.15$ s (green, dot-dashed line) and $t=2.50$ s (red, dotted line). (Figure taken from Reid & Ratcliffe, 2014).

the total energy density, can be expressed as follows (Reid & Ratcliffe, 2014),

$$\frac{\partial f(v, t)}{\partial t} = \frac{4\pi^2 e^2}{m_e^2} \frac{\partial}{\partial v} \left(\frac{W}{v} \right) \frac{\partial f(v, t)}{\partial v} \quad (1.2)$$

$$\frac{\partial W(v, t)}{\partial t} = \frac{\pi \omega_p}{n_e} v^2 W \frac{\partial f(v, t)}{\partial v} \quad (1.3)$$

Equation 1.3 shows that the growth rate of Langmuir waves is proportional to $\frac{\partial f(v, t)}{\partial v}$, hence a positive gradient in the Maxwell Boltzmann distribution leads to a growth in Langmuir waves. The right hand side of Eq. 1.2 has a diffusion operator $D = \frac{W}{v}$. This states that the transfer of energy from particles to waves and back leads to the distribution function being smoothed out and eventually becoming a plateau. The evolution of $f(v, t)$ and $W(v, t)$ with time is shown in Figure 1.7. Figure 1.7 shows how the plateau in the distribution function and a broadening in the spectral energy density develop as time progresses.

1.2.2 Wave-Wave Interaction

Wave-wave interaction concerns the processes by which three types of waves interact. These are: transverse (T) waves, Langmuir (L) waves and ion sound (S) waves, and have

the following, respective dispersion relations,

$$\omega = (\omega_p^2 + k^2 c^2)^{\frac{1}{2}}$$

$$\omega \cong \omega_p + \frac{3k^2 V_e^2}{2\omega_p}$$

$$\omega = kv_s$$

where V_e is the thermal velocity of electrons in the plasma, v_s is the ion sound speed and k is the wave vector. Only transverse waves with $\omega > \omega_p$ can escape and thus a plasma emission mechanism is a process that generates these transverse waves.

As mentioned in Section 1.1.5, Type III bursts have a harmonic structure associated with plasma emission at the plasma frequency and the second harmonic. Both of these transverse waves are formed in different three wave processes that will now be discussed. In a plasma, due to scattering from other wave modes and ions in the plasma, a wave mode can be changed from one to the other. This is expressed in the equation

$$\sigma \rightleftharpoons \sigma' + \sigma''$$

where σ , σ' and σ'' represent different wave modes. Conservation of energy and momentum state,

$$\omega^\sigma(k) = \omega^{\sigma'}(k') + \omega^{\sigma''}(k'')$$

$$k = k' + k''$$

where $\omega^\sigma(k)$ is the frequency of a particular wave mode with the wave vector k . For Langmuir (L), ion sound (S) and transverse (T) wave modes the allowed processes are $L+S \rightarrow L'$, $L+S \rightarrow T$, $T+S \rightarrow L$, $T+S \rightarrow T'$ and $L+L' \rightarrow T$. Of these $L+S \rightarrow T$, $L \rightarrow T+S$ are responsible for fundamental emission while harmonic emission is associated with the three wave process $L+L' \rightarrow T$.

Originally Ginzburg & Zhelezniakov (1958) considered fundamental emission to be due to Langmuir waves scattering off of thermal ions in the plasma. It is now commonly accepted that the biggest cause of fundamental emission is due to the three wave processes of a Langmuir wave coalescing with an ion sound wave generated by $L \rightarrow L'+S$ or when a Langmuir wave decays into an ion sound wave and an electromagnetic transverse wave. The process $L \rightarrow T+S$ can be visualised as in Figure 1.8. In solar radio physics it is often assumed that $k_L \gg k_T$, knowing this and that the wave vectors must satisfy $\mathbf{k}_L \pm \mathbf{k}_s = \mathbf{k}_T$ (+ for $L+S \rightarrow T$, - for $L \rightarrow T+S$) implies $\mathbf{k}_s \approx \mp \mathbf{k}_L$

Second harmonic emission occurs when two Langmuir waves coalesce in the process $L+L' \rightarrow T$, shown in Figure 1.9. Conservation of momentum requires that $\mathbf{k}_L + \mathbf{k}'_L = \mathbf{k}_T$ and for second harmonic (H) generation, $k_T = k_H \approx \frac{\sqrt{3}\omega_p}{c}$. The phase speed v_ϕ of

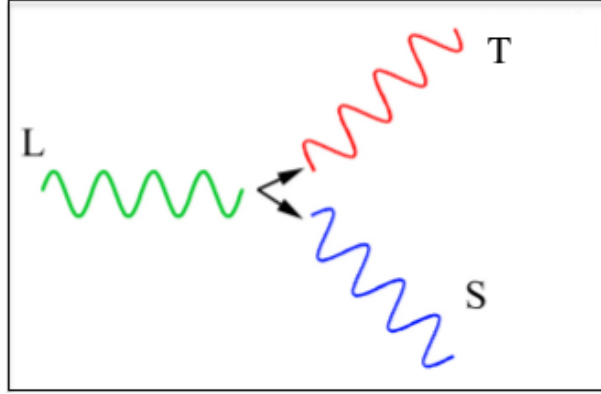


Figure 1.8: A three wave process of fundamental plasma emission $L \rightarrow T + S$. A Langmuir wave decaying into an ion sound wave and an electromagnetic transverse wave at the plasma frequency. (Figure adapted from Solar (interplanetary) Radio Bursts: the Generation of Radio Waves, an oral presentation by David Malaspina at the Jean Louis Steinberg International Workshop on Solar, Heliospheric and Magnetospheric Radioastronomy, November 2017)

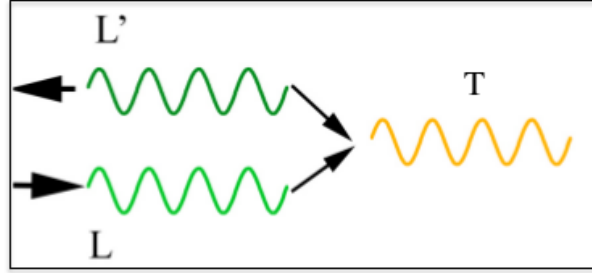


Figure 1.9: Three wave process of second harmonic plasma emission $L + L' \rightarrow T$. A Langmuir wave (L) and a backwards propagating Langmuir wave (L') coalesce to form a transverse wave (T) at $2\omega_p$. (Figure adapted from Solar (interplanetary) Radio Bursts: the Generation of Radio Waves, an oral presentation by David Malaspina at the Jean Louis Steinberg International Workshop on Solar, Heliospheric and Magnetospheric Radioastronomy, November 2017)

Langmuir waves is much less than $\frac{c}{\sqrt{3}}$ meaning that $k_L \gg k_T$ which results in $\mathbf{k}_L \approx -\mathbf{k}'_L$. This means that for a transverse wave at the second harmonic to be created, two Langmuir waves must coalesce almost exactly head on. These backward propagating Langmuir waves are generated: in the three wave processes of $L + S \rightarrow L'$ and $L \rightarrow L' + S$; scattering off of thermal ions; and refraction at density inhomogeneities.

1.3 Radio Interferometry

There are two limiting factors in modern-day optical astronomy, diffraction and atmospheric conditions. The latter has been overcome using advanced adaptive optics techniques or avoided entirely by putting telescopes in space. This leaves diffraction as a fundamental limit to the resolving power of any telescope.

Rayleigh's criterion states that for an object to be resolved, the maximum of its interference pattern must overlap the minimum of another. This leads to the mathematical

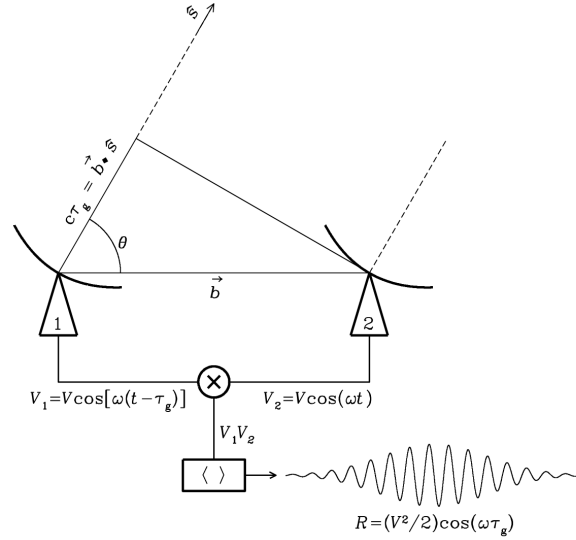


Figure 1.10: A two element interferometer separated by a baseline \vec{b} . The signal from each antenna is correlated by first multiplying the two voltages then time averaging them.

relationship (assuming a circular aperture),

$$\theta \approx 1.22 \frac{\lambda}{D}$$

where θ is the angular resolution of an object, λ is the wavelength observed in and D is the aperture diameter of the telescope. The Hubble Space Telescope, with a diameter of 2.4 m and observing in near IR therefore has an angular resolution of ~ 0.05 arcseconds. For a radio telescope observing 10 m waves to have the same resolution, ignoring atmospheric effects, it would need an aperture diameter of 41000 km. Building a single dish of this size is practically impossible. Fortunately, because radio waves are so large, they can be detected at multiple locations at great distances from each other and the original signal pieced back together. This idea forms the basis of radio interferometry. The mathematical framework for this is *slightly* more complicated than this simple view so to explain it the most fundamental radio interferometer, the two element interferometer, is described.

Consider two radio antennae, 1 and 2, separated by a distance \vec{b} , this is the antenna baseline and is equivalent to the diameter of a classic telescope. A radio wave approaching the antennae from direction \hat{s} will hit antenna 2 first then antenna 1 after a time delay of τ_g such that,

$$\tau_g = \frac{\vec{b} \cdot \hat{s}}{c}$$

where c is the speed of light. The output from each antenna is a voltage $V_1 = V \cos \omega(t - \tau_g)$ and $V_2 = V \cos \omega t$. The total response, R_c of the interferometer is the correlation or mul-

multiplication and time average of these two voltages, $\langle V_1 V_2 \rangle$.

$$R_c = \langle V_1 V_2 \rangle = \frac{V^2}{2} \cos \omega \tau_g$$

Furthermore, if a 90° phase shift is added to the output of one antenna, the response becomes

$$R_s = \langle V_1 V_2 \rangle = \frac{V^2}{2} \sin \omega \tau_g$$

A complex visibility can be defined as the complex sum of the two responses $V(\hat{\mathbf{s}}) = R_c - iR_s$. Using Euler's formula, the complex visibility of an extended source is given by:

$$V(\hat{\mathbf{s}}) = \int I(\hat{\mathbf{s}}) \exp(-i\omega \tau_g) d\Omega = \int I(\hat{\mathbf{s}}) \exp(-2\pi i \frac{\vec{\mathbf{b}} \cdot \hat{\mathbf{s}}}{\lambda}) d\Omega \quad (1.4)$$

where I is the sky brightness distribution. In more conceptual terms, the complex visibility is the Fourier transform of the sky brightness distribution.

Equation 1.4 can be rewritten as a function of the uvw coordinate system and using the directional cosine coordinate system for source position on the sky.

$$V(u, v) = \int I(l, m) \exp(-2\pi i(ul + vm)) dl dm \quad (1.5)$$

The coordinate system commonly used throughout radio interferometer is the l, m, n or directional cosine coordinate system. This determines a position on the sky in terms of the direction cosines to that position. Here l, m, n are defined as

$$l = \cos \delta \sin \Delta\alpha, \quad m = \sin \delta \cos \delta_0 - \cos \delta \sin \delta_0 \cos \Delta\alpha, \quad n = \sqrt{1 - l^2 - m^2}$$

where δ, δ_0 are the declinations of an object and the phase centre, respectively, and $\Delta\alpha = \alpha - \alpha_0$ is the difference between the right ascension of the object and phase centre (direction of the primary beam).

Baselines in radio interferometry are described using the uvw coordinate system defined as

$$\begin{bmatrix} u \\ v \\ w \end{bmatrix} = \frac{1}{\lambda} \begin{bmatrix} \sin H & \cos H & 0 \\ -\sin \delta \cos H & \sin \delta \sin H & \cos \delta \\ \cos \delta \cos H & -\cos \delta \sin H & \sin \delta \end{bmatrix} \begin{bmatrix} B_x \\ B_y \\ B_z \end{bmatrix}$$

Here, H is the hour angle of an object, δ is its declination, $\mathbf{B} = (B_x, B_y, B_z) = (x_2 - x_1, y_2 - y_1, z_2 - z_1)$ is the baseline or distance between two antennae and λ is the wavelength of the radio waves being observed.

1.3.1 Beam-forming

In its most simple terms, beamforming means pointing a phased array in a particular direction. It involves correcting for phase difference between the “phase centre” of the beam and the position of the source of interest for each baseline and then summing it all together. In order to beamform, one must account for the phase difference between the phase centre (where the beam is physically pointing) and the source (at an angular coordinate of (l, m) with reference to the phase centre). As above, this phase difference for a baseline pq is given by,

$$\kappa_{pq} = 2\pi(u_{pq}l + v_{pq}m + w_{pq}(n - 1))$$

In order to correct for the phase difference and steer the beam, data for baseline pq is multiplied by the complex weight $e^{-i\kappa_{pq}}$, this is repeated for all baselines and finally all data is summed.

- Appleton, E. & Hey, J. 1946, The London, Edinburgh, and Dublin Philosophical Magazine and Journal of Science, 37, 73
- Aschwanden, M. J. 2004, Physics of the Solar Corona
- Bastian, T. S. 1994, The Astrophysical Journal, 426, 774
- Boischot, A. & André. 1957, Comptes Rendus de l'Académie des Sciences, Paris, Vol. 244, p. 1326-1329, 244, 1326
- Clarke, B. P., Morosan, D. E., Gallagher, P. T., et al. 2019 [[arXiv]1901.07424]
- Cliver, E. W. & Ling, A. G. 2009, The Astrophysical Journal, 690, 598
- Ellis, G. 1969, Australian Journal of Physics, 22, 177
- Foukal, P. V. 2004, Solar Astrophysics, 480
- Ginzburg, V. L. & Zhelezniakov, V. V. 1958, Astronomicheskii Zhurnal, 35, 694
- Gopalswamy, N. & Thompson, B. 2000, Journal of Atmospheric and Solar-Terrestrial Physics, 62, 1457
- Kontar, E. P., Yu, S., Kuznetsov, A. A., et al. 2017, Nature Communications, 8, 1515
- Malville, J. M. & M., J. 1962, The Astrophysical Journal, 135, 834
- Mann, G. 1995, in Lecture Notes in Physics, Berlin Springer Verlag, Vol. 444, Coronal Magnetic Energy Releases, ed. A. Benz & A. Krüger, 183
- McConnell, D. 1980, Publications of the Astronomical Society of Australia, 4, 64
- McLean, D. J. & Labrum, N. R. 1985, Cambridge and New York, Cambridge University Press, 1985, 527 p. For individual items see A87-13852 to A87-13867.
- Melnik, V. N., Konovalenko, A. A., Rucker, H. O., et al. 2010, Solar Physics, 264, 103
- Melrose, D. B. 1982, Solar Radio Storms, CESRA Workshop #4, 182
- Melrose, D. B. 1987, Solar Physics, 111, 89
- Morosan, D. E., Gallagher, P. T., Zucca, P., et al. 2015, Astronomy & Astrophysics, 580, A65
- Nelson, G. & Melrose, D. 1985, in Solar Radiophysics: Studies of Emission from the Sun at Metre Wavelengths, ed. D. McLean & N. Labrum, 333-359
- Reid, H. A. & Kontar, E. P. 2017, Astronomy and Astrophysics, 606 [[arXiv]1706.07410]
- Reid, H. A. S. & Ratcliffe, H. 2014, Research in Astronomy and Astrophysics, 14, 773
- Reiner, M., Kaiser, M., Fainberg, J., Bougeret, J.-L., & Stone, R. 1997, in ESA Special Publication, Vol. 415, Correlated Phenomena at the Sun, in the Heliosphere and in Geospace, ed. A. Wilson, 183
- Riddle, A. C. 1974, Solar Physics, 35, 153
- Smerd, S., Sheridan, K., & Stewart, R. 1974, in IAU Symposium, Vol. 57, Coronal Disturbances, ed. G. Newkirk, 389
- Vedenov, A. A. 1963, Journal of Nuclear Energy. Part C, Plasma Physics, Accelerators, Thermonuclear Research, 5, 169
- Vršnak, B., Magdalenic, J., Aurass, H., & Mann, G. 2002, Astronomy & Astrophysics, 396, 673
- Wild, J. P. 1950, Australian Journal of Chemistry, 3, 399
- Wild, J. P. & McCready, L. L. 1950, Australian Journal of Scientific Research A, vol. 3, p.387, 3, 387
- Wild, J. P., Sheridan, K. V., & Trent, G. H. 1959, URSI Symp. 1: Paris Symposium on Radio Astronomy, 9, 176
- Zucca, P., Carley, E. P., McCauley, J., et al. 2012, Solar Physics, 280, 591